HYPERBOLIC PARABOLOID SHELLS MADE OF DIAGONAL LAMINATED TIMBER ELEMENTS

Matthias Arnold[1], Philipp Dietsch[2], Stefan Winter[3]

ABSTRACT: This paper deals with the design, calculation, and construction of hyperbolic paraboloid shells made from mass timber elements. Considering the geometrical definition, hyperbolic paraboloid shells can be described as doubly ruled surfaces and can therefore be assembled from twisted rectangular plates.

The membrane theory of the hyperbolic paraboloid shell is derived and compared to previous analytical approaches. A challenge is the realization of the shell using the orthotropic material timber. Therefore, the torsional stiffness of multi-layered mass timber elements is determined by means of analytical and experimental investigations. Taking into account the semi-rigid connection between the layers, resulting in additional shear deformations, nailed and diagonal laminated timber elements are investigated towards the construction of HP-shells.

KEYWORDS: hyperbolic paraboloid shell (HP-shell; hypar), membrane theory, diagonal laminated timber (DLT), nailed laminated timber (NLT), semi-rigid connections, laminate theory, torsional stiffness

1 INTRODUCTION

1.1 BACKGROUND

The application of HP-shells made of timber found its temporary peak around 1970, for example at the exhibition pavilion for the Federal Garden Show in Dortmund, Germany, 1969. For the assembly of the shell, five layers of single laminations were laid on top of each other and fixed by mechanical fasteners, e.g. nails. Timber shells offer many advantages, for example the fast erection, the low weight, and the high quality of the surface. Experiments with timber HP-shells were first carried out at University of Kansas in 1956 [1]. A similar project was realized in Stuttgart in 1963 [2] (Fig. 1).
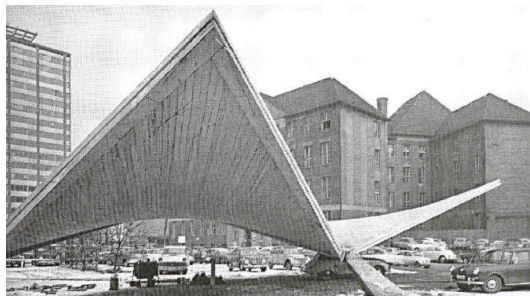

Figure 1: *Experimental timber HP-shell (span l′ = 15.0 m) in front of Stuttgart University, 1963* [2]

In general, a hypar can be described mathematically as a translational surface (fictive parabolas in x′ and y′ direction, acting in tension and compression only, Fig. 2) and as doubly ruled surface (straight lines in x or y direction forming rectangular plate elements, acting in in-plane shear only, Fig. 3).
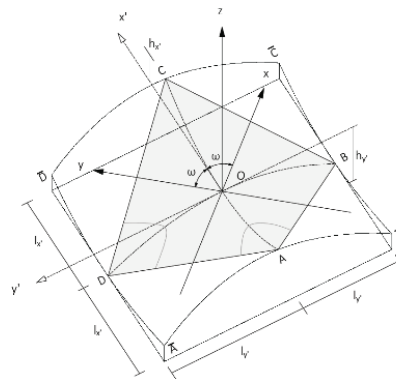

Figure 2: *Hypar described by a translational surface* [3]

The translational surface is given by Eq. (1). By rotating the x′ and y′ axis by the angle ω, to correspond with the asymptotes of the hyperbola, a new description based on the global x and y axis is introduced—see Eq. (2) [4].

$$z = \frac{h_{x'}}{(l_{x'})} \cdot x'^2 - \frac{h_{y'}}{(l_{y'})} \cdot y'^2 \qquad (1)$$

$$z = \frac{4 \cdot sin^2\omega \cdot h_{y'}}{(l_{y'})^2} \cdot x \cdot y \qquad (2)$$

$$z = \frac{h_{y'}}{(l_{y'})^2} \cdot 2 \cdot x \cdot y = \frac{h}{ab} \cdot x \cdot y = k \cdot x \cdot y \qquad (3)$$

A symmetrical hypar ($h_{y'} = h_{x'}$) over a square plane projection ($2\omega = 90°$) can therefore be described by Eq. (3) using the global x and y axis [5]. Fig. 3 show that

[1]Matthias Arnold, Technical University of Munich, Germany, matthias.arnold@tum.de
[2]Philipp Dietsch, Karlsruhe Institute of Technology, Germany, dietsch@kit.edu

[3]Stefan Winter, Technical University of Munich, Germany, winter@tum.de

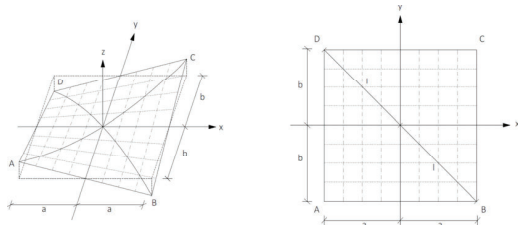the ruled surface can be assembled from single, twisted rectangular elements.

Figure 3: Hypar described by a ruled surface [3]

1.2 OBJECTIVE

The objective of the research presented is to create a HP-shell from prefabricated, large-scale NLT or DLT plates and thus to create HP-shells with a high degree of prefabrication. Thereby the elements remain plane during production and get twisted on the construction site, by connecting them to edge beams. In a second construction step, the elements are connected to the adjacent elements, taking the in-plane shear forces n_{xy}.
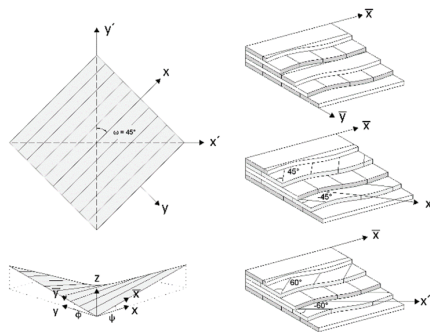

Figure 4: Exemplary layups of DLT elements according to the geometry of the shell in the plane projection

Depending on the fictive compression and tension parabolas, the layup of the mass timber elements can be adapted to the principle membrane forces ($n_{x'}$ and $n_{y'}$) by rotating individual layers during production. The resulting multi-layered element is a balanced and symmetric laminate (Fig. 4, right). This means, for each $+\theta$ ply in the laminate there is an equally thick $-\theta$ ply (referred to the symmetry axis). The layers of the laminate are a mirror image about the geometrical midplane.

Within previous research [6; 7] mass timber elements featuring diagonally arranged layers had been defined as DLT. In general, the diagonal layer arrangements of DLT elements lead to an increase of the torsional stiffness compared to conventional CLT elements. This is also due to the high out-of-plane shear stiffnesses S_{xz} and S_{yz} of DLT [8]. In case of the application on HP-shells, the DLT elements should provide a small torsional stiffness in order to not disturb the membrane stress state due to the additional load case of torsion caused by the twisting of the elements. Therefore, a semi-rigid connection of the layers by mechanical fasteners (nails) is introduced.

2 SERIES INVESTIGATED

2.1 LAYUPS

Tab. 1 gives the layup and stacking sequence of the specimens investigated. DLT_n is the designation for nailed DLT. All specimens are made of spruce (see Chapter 2.2). In addition, the number n of specimens investigated is given.

Table 1: Specimens per Series for the mechanical testing

series		n	[1)]orientation θ [°]	t [mm]
O1	CLT	4	0°, 90°, 0°, 90°, 0°	100
O2	NLT	4	0°, 90°, 0°, 90°, 0°	105
O3	CLT	2	0°, 90°, 0°	60
O4	NLT	3	0°, 90°, 0°	63
D1	[2)]DLT±45°_n	3	0°, 45°, 90°, -45°, 0°	105
D2	[2)]DLT±30°_n	3	0°, 30°, 90°, -30°, 0°	105
D3	DLT±45°	3	0°, 45°, 90°, -45°, 0°	100
D4	DLT±30°	3	0°, 30°, 90°, -30°, 0°	100

[1)]layer orientation referred to the local $\bar{x}$ axis of the specimens
[2)]DLT specimens with semi-rigidly connected layers using nails

2.2 MATERIAL PROPERTIES

The CLT elements were produced using material properties according to ETA 20/0023 [9]. The DLT elements were produced using according to ETA 16/0055 [10]. Each layer of the CLT has a thickness of $d = 20\ mm$. The laminations are not edge-glued and the board width is $b = 180\ mm$. The modulus of elasticity (MoE) was cross-checked by compression tests according to EN 408 [11] and was $E_{c,0,mean} = 10282$ MPa (COV 0.56 %). The NLT and DLT_n elements were produced according to ETA 15/0760 [12]. Each layer has a thickness of $d = 21\ mm$. The MoE was determined by four-point bending tests according to EN 408 [11] and was $E_{m,0,mean} = 11044$ MPa (COV 1.21 %).

At the beginning of the mechanical testing the moisture of each specimen was determined by means of ram in electrodes at a depth of approximate 15 mm. On each specimen 5 measurements were taken. The mean value $u_{mean,15mm}$ of the initial moisture content was 11.2 % (COV 7.6 %). The moisture content u of all specimen was in the range of $12 \pm 2\%$. The mean value of the density at $u = 12\%$ was exemplary determined for series O1 according to EN 384 [13]. The mean value ρ_{mean} was 458 kg/m³ (COV 4.3 %).

2.3 CONSIDERATION OF THE NAILING

The layers of the NLT and DLT_n are connected to the underlying layers with aluminium grooved nails ($t = 2.5\ mm$) [12]. During production, the nailing unit moves over the layers at the same predefined spaces and shoots the single nails into the laminations. Using a Monte-Carlo-Simulation (MC-simulation), the probability of inserting a number m of nails per crossing point of the single laminations is calculated statistically. Nails between the edges of the boards or outside the required minimum edge distance must not be used for the calculation of the stiffness properties of the composites (circled nails in Fig. 5).
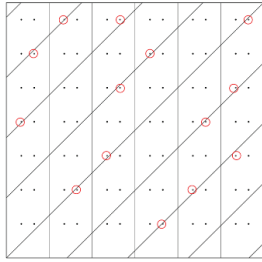
Figure 5: Exemplary distribution of nails for joining two layers (crossing angle at 45°) using statistical evaluation

Determining the statistical distribution of nails per crossing-point, an average effective number of nails per crossing of two layers (1.20 m / 1.20 m) can be calculated (mean value). The result of the simulation is verified by counting the actual nails per layer and crossing-point on the specimens (Fig. 6).
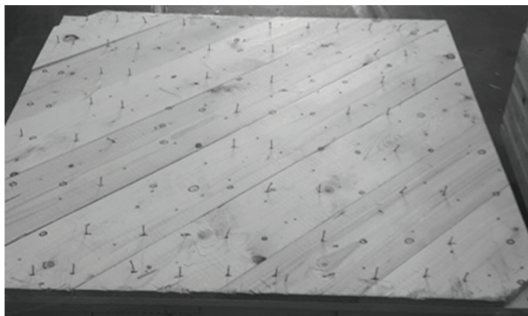
Figure 6: Exposed nail pattern between two layers, crossing under 45°

Tab. 2 compares the results of the MC-simulation to the nails counted for two layers crossing under 45°, 60° (30°), and 90°. The number of nails that can be effectively applied per crossing-point are used for the calculation of the stiffness values.

Table 2: Effective number of nails per crossing of two layers of the NLT and DLT_n specimens

crossing angle	crossing points with n nails (MC-Simulation) [%]					calculated effective nails (1.20/1.20)	[1]counted effective nails (1.20/1.20)
	$m=$ 0	$m=$ 1	$m=$ 2	$m=$ 3	$m=$ 4		
45°	7,1	7,1	28,6	42,9	14,7	78	80
60°	5,3	0,0	15,8	52,6	26,3	80	80
90°	14,3	9,5	52,4	23,8	23,8	111	114

[1]mean value of the counted nails at the crossing of two layers (1.20/1.20)

3 ANALYTICAL INVESTIAGIONS

3.1 STIFFNESS PROPERTIES OF DLT AND NLT

The stiffness properties of multi-layered timber elements can be determined by the stiffness properties of the individual layers i and their interaction as a composite. The laminate theory of orthogonally glued CLT can be taken from several previous publications [14; 15]. Laminates are characterized by their response to mechanical loading, which is associated with a description of the coupling behavior. The matrix notation of the law of elasticity on the plate element consists of submatrices. These refer to the extensional stiffness A, the bending-extension coupling stiffness B, and the bend-twist coupling stiffness D (*ABD*-relation). Taking into account the transverse shear deformations, which are decoupled from the *ABD*-relation, a fourth submatrix E has to be introduced [15]. The stiffness parameters can be taken from the *ABD-E* stiffness matrix. For antisymmetric, balanced laminates, simplifications within the stiffness matrix can be made ($A_{16} = A_{26} = D_{16} = D_{26} = B_{11} = B_{12} = B_{22} = B_{66} = E_{54} = 0$) which leads to the stiffness matrix given by Eq. (4).

$$[Q] = \begin{bmatrix} A_{11} & A_{12} & 0 & 0 & 0 & B_{16} & 0 & 0 \\ A_{21} & A_{22} & 0 & 0 & 0 & B_{26} & 0 & 0 \\ 0 & 0 & A_{66} & B_{61} & B_{62} & 0 & 0 & 0 \\ 0 & 0 & B_{16} & D_{11} & D_{12} & 0 & 0 & 0 \\ 0 & 0 & B_{26} & D_{21} & D_{22} & 0 & 0 & 0 \\ B_{14} & B_{24} & 0 & 0 & 0 & D_{66} & 0 & 0 \\ 0 & 0 & 0 & 0 & 0 & 0 & E_{55} & 0 \\ 0 & 0 & 0 & 0 & 0 & 0 & 0 & E_{44} \end{bmatrix} \quad (4)$$

For CLT and DLT elements, the entries for S_{xz} (E_{44}) and S_{yz} (E_{55}) have to be multiplied by shear-correction factors k_z. A possible calculation of the shear-correction factors in the global x and y direction is based on the Timoshenko Beam Theory [16] according to Eq. (5). The derivation of Eq. (5) is based on the principle of virtual displacements (method of consistent deformations; force method) and the equilibrium between shear and bending stiffnesses over the cross-section [17].

$$\frac{1}{k_z} = \frac{\sum G_{iz} A_i}{\left(\int_{-\frac{t}{2}}^{\frac{t}{2}} E_i(z) z^2 \, dz \right)^2} \cdot \int_{-\frac{t}{2}}^{\frac{t}{2}} \frac{\left(\int_z^{\frac{t}{2}} E_i(z) z \, dz \right)^2}{G_{iz}(z)} dz \quad (5)$$

For NLT and DLT_n on the other hand, the semi-rigid connection of the layers has to be taken into account; the contribution of the layers—especially the transverse layers—on the shear deformations become marginal. Therefore, the laminate theory and shear-strain relation stays no longer valid. DIN EN 1995-1-1/NA [18] provides an analytical method for the calculation of out-of-plane shear stiffness values of semi-rigid connected mass timber elements by Equations (NA.40) and (NA.42). The calculation is based on the *Shear Analogy Method* [19] and considers a constant shear flow over the effective heights (shear area) a (Eq. (6)).

$$\frac{1}{S_{xz/yz}} = \frac{1}{a_{x/y}} \cdot \left[\sum_{i=1}^{n-1} \frac{1}{k_{x,i/y,i}} + \frac{d_1}{2G_{xz/yz}} + \sum_{i=1}^{n-1} \frac{d_i}{G_{xz,i/yz,i}} + \frac{d_n}{2G_{xz/yz}} \right] \quad (6)$$

with
$n =$ number of layer [/]
$a =$ effective heigths [19]
$G_{xz,i/yz,i} =$ shear modulus of the respective layer,
(for layer arranged under 45°, $G_{45} = 370 \, MN/m^2$)
$d_i =$ layer thickness [mm]]
$k_i =$ slip modulus between the layers [N/mm]

ETA 15/0760 [12] gives an approximate analytical method for the calculation of the out-of-plane shear stiffness values of NLT and DLT_n, taking into account the number of layers n, the effective number of nails per crossing-point m (see Tab. 2) and the initial slip modulus K of the nails. Therefore, the slip modulus k between the layers—see Eq. (6)—is substituted, using Eq. (7).

$$\sum_{i=1}^{n-1} \frac{1}{k_{x,i/y,i}} = \sum_{i=1}^{n-1} \left(\frac{1}{f} \cdot \frac{1}{m \cdot \left(\frac{K}{b_x \cdot b_y} \right)} \right) \quad (7)$$

with
m = number of nails per crossing point [/]
K = initial slip modulus of a single nail [N/mm]
b_x = b_y = board width [mm]
$f = 1,25$ for $m = 4$, and $f = 1,5$ for $m = 2$

3.2 MEMBRANE FORCES OF THE HP-SHELL

3.2.1 Equilibrium conditions and differential equation

Pucher [20] established a method for the calculation of membrane forces in arbitrary shell structures by transferring stress resultants on infinitesimal elements, to their plane projection (Fig. 7). The plane projection is in the state of equilibrium in x and y direction. Fig. 7 shows the geometric relationships $tan\varphi = \partial z / \partial x$ and $tan\psi = \partial z / \partial y$ introducing a third equilibrium in z-direction.
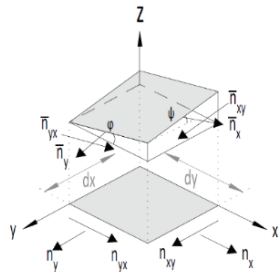

Figure 7: Transfer of stress resultants to the plane element

Eq. (8) gives the equilibrium conditions on the plane element.

$$\bar{n}_x = n_x \cdot \frac{cos\varphi}{cos\psi} \quad ; \quad \bar{n}_y = n_y \cdot \frac{cos\psi}{cos\varphi} \quad ;$$
$$n_{xy} = \bar{n}_{xy} \quad ; \quad n_{yx} = \bar{n}_{yx} \quad (8)$$

The calculation of stress resultants on the infinitesimal shell elements is based on the assumption of the membrane theory for thin shells (transverse shear forces, bending moments, and torsional moments are neglected [21]). This means that the shell is statically determined; Three unknown stress resultants face three equilibrium conditions ($\sum F_x = 0, \sum F_y = 0, \sum F_z = 0$). Hereby, the stress resultants can be calculated without material or kinematic conditions. The derivatives of the equilibrium relations (Eq. (9)) are inserted into the *Airy Stress Function F* (Eq. (10)) to achieve the ordinary differential equation (Eq. (11)) [20].

$$n_x = \frac{\partial^2 F}{\partial y^2} - \int p_x d_x \ ;$$
$$n_y = \frac{\partial^2 F}{\partial x^2} - \int p_y d_y \ ; \quad (9)$$
$$n_{xy} = n_{yx} = -\frac{\partial^2 F}{\partial x \partial y}$$

$$F = \frac{\partial^2 F}{\partial y^2} \frac{\partial^2 z}{\partial x^2} - 2 \frac{\partial^2 F}{\partial x \partial y} \frac{\partial^2 z}{\partial x dy} + \frac{\partial^2 F}{\partial x^2} \frac{\partial^2 z}{\partial y^2} \quad (10)$$

$$F = -p_z + p_x \frac{\partial z}{\partial x} + p_y \frac{\partial z}{\partial y} + \int p_x d_x \frac{\partial^2 z}{\partial x^2} + \int p_y d_y \frac{\partial^2 z}{\partial y^2} \quad (11)$$

The surface equation $z = k \cdot xy$ (Eq. (3)) is derived according to Eq. (11) to receive the ordinary differential equation of a hyperbolic paraboloid (Eq. (12)) [22]:

$$-2k \cdot \frac{\partial^2 F}{\partial x \partial y} = -p_z + p_x \cdot y \cdot k + p_y \cdot x \cdot k \quad (12)$$

To derive the membrane forces n_x and n_y as well as the in-plane shear forces n_{xy} the equilibrium conditions (Eq. (8)) are solved. A uniform loading p_z leads to in-plane membrane forces n_{xy} only, within the global x-y coordinate system (Eq. (13)).

$$n_{xy} = \frac{-p_z + p_x \cdot y \cdot k + p_y \cdot x \cdot k}{2k} \quad (13)$$

The membrane forces n_{xy} are equivalent to normal forces in the x´-y´ coordinate system. This means that the in-plane shear force n_{xy} can be split into normal forces $n_{x'}$ and $n_{y'}$ (normal forces acting along the fictive compression and tension parabolas of the HP-shell). Therefore, the membrane forces can be calculated on the plane projection of an infinitesimal shell element, taking into account the boundary conditions of the edges. The main boundary conditions are classified into free edges ($n_x = n_{xy} = 0$), linear supported edges (edge beams; $n_x = n_y = 0$ and $n_{xy} \neq 0$) and clamped/ edges ($n_x = n_{xy} \neq 0$) [23].

3.2.2 Simplified calculation method

The basic idea of Parme in 1960 [24] was to describe the load transfer in HP-shells by fictive compression and tension parabolas (Fig. 8). This idea was further developed by Hempel in 1967 [25] and Krauss in 1969 [26].
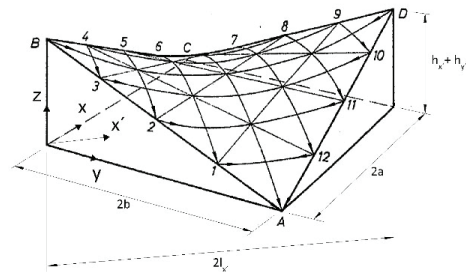

Figure 8: Distribution of the shell into compression and tension parabolas [26]

Since the solution of the membrane forces are a function the loading, Parme [24] assumed that a uniform load q_z [kN/m²] on a double symmetric HP-shell over a square projection gets equally distributed between two perpendicular parabolas.

For the boundary condition of linear supported edges ($n_x = n_y = 0$ and $n_{xy} \neq 0$) the normal force N—acting along the edge beams—result from the calculation of the horizontal and vertical reactions of the compression and tension parabolas, taking into account load-distribution factors $\chi_{x'/y'}$ (Eq. (14) and (15)) [26].

$$H_{x'/y', \ n} = \chi_{x'/y'} \cdot q_z \cdot \frac{\left(2 \cdot l_{x'/y',n}\right)^2}{8 \cdot h} \tag{14}$$

$$V_{x'/y', \ n} = \chi_{x'/y'} \cdot q_z \cdot \frac{2 \cdot l_{x'/y',n}}{2} \tag{15}$$

$with$

$$\chi_{x'} = \frac{1}{1 + \dfrac{\sum EA_{y',i}}{\sum EA_{x',i}} \cdot \dfrac{l_{x'}^4}{l_{y'}^4}} \quad ; \quad \chi_{y'} = 1 - \chi_{x'}$$

If the distribution of the axial rigidity is the same in x´ and y´ directions ($\chi_{x'} = \chi_{y'} = \frac{1}{2}$)—which is the case for the chosen series (Tab.1)—the shear force n_{xy} equals the resultant R of the horizontal reactions of the fictive compression and tension parabolas (Fig. 9).
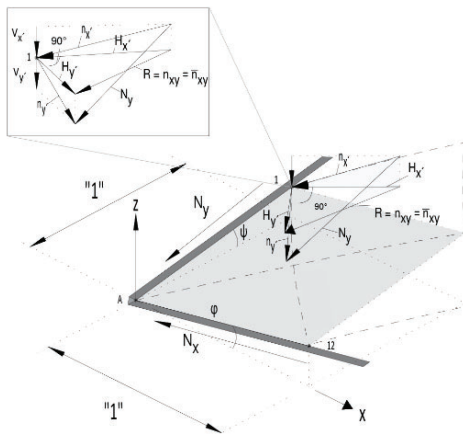

Figure 9: *Resulting forces in the HP-shell and in the edge beams under a uniformly distributed load p*

The geometric relationship of Fig. 9 can also be proven mathematically by comparing n_{xy}—calculated from $n_{x'}$ and $n_{y'}$ according to Pythagoras' Theorem—with n_{xy} according to the membrane theory under a uniform surface load q_z.

4 EXPERIMENTAL INVESTIGATIONS

4.1 TEST SETUP

After analytical investigations of the torsional stiffness properties, NLT, CLT, and DLT specimens featuring layups according to Tab. 1 with a side length $a = 1200 \ mm$ are twisted in biaxial bending tests. The aim is to determine the torsional stiffness properties of the various specimens from the deformation of the elements under an external point-load, in order to make statements on the additional out-of-plane load case of torsion at the assembly of HP-shells. Parts of the results of the mechanical testing on CLT and DLT were already published within [7] and [8]. Fig. 10 shows the test setup of the biaxial bending test.

The point-load, directed vertically downwards, is applied to the free corner of the specimens by a hydraulic cylinder. The load-application point as well as the supports are realized by steel plates (120/120/12 mm). They each are articulated and offset inwards by 100 mm from the free edges of the specimens. No reinforcement for compression perpendicular to the grain stresses in form of self-tapping screws is applied.
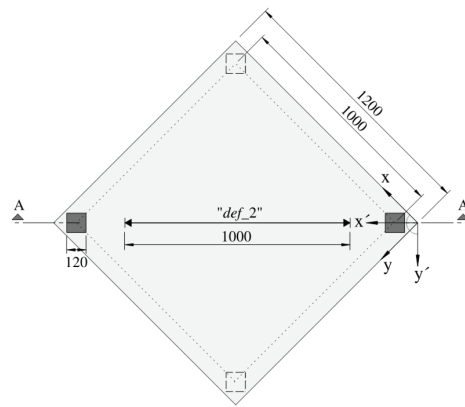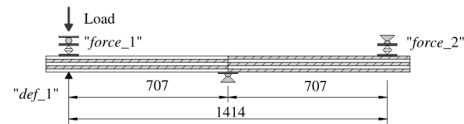

Figure 104: *Biaxial bending tests to determine the torsional stiffness of CLT, DLT, and NLT specimens*

The applied loading "$force\_1$" (point-load F) as well as at the reaction force on the opposite support "$force\_2$" are measured by force transducers. Deflection "def_1" (deflection w in z direction) is measured using a rope extensometer which is attached at the opposite side of the load-introduction point at the bottom of the test specimens. In addition, the change in the curvature κ_{xy} is measured determining the arc length "def_2" over 1000

mm by means of a second rope extensometer on the upper side of the specimens. The mechanical testing is carried out deformation-controlled. This means that each test specimen is loaded until a unit-deflection w (def_1) of $100\ mm$ (geometrical limit imposed by geometry of load-introduction) or failure. All specimens are loaded with a constant feed rate of about $0.30\ mm/s$. The corresponding forces F ("$force\_1$" = "$force\_2$") are measured as a function of the time.

4.2 TEST RESULTS AND COMPARISON TO AN ANALYTICAL APPROACH

Fig. 11 exemplary gives the load-deflection diagrams for the NLT and DLT_n series. Load-deflection diagrams for the CLT and DLT series can be taken from [7].
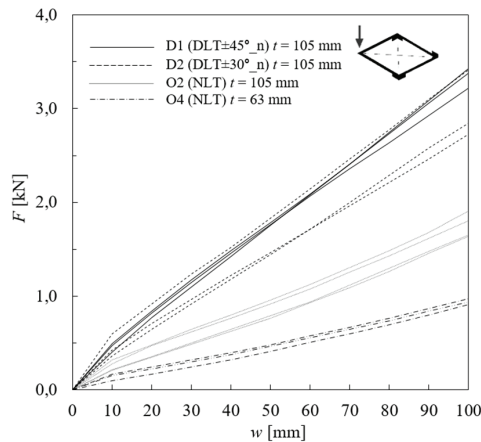

Figure 11: Load-deflection diagrams of the NLT and DLT_n specimens under biaxial bending

The load-deformation curves show a kink when overcoming the static friction force in the joint between the board layers $(F_{st,fr} < 0.2 F_{w_{100}})$. The torsional stiffness for each specimen is calculated within the linear elastic range $0.2 F_{max}$ $(0.2 F_{w_{100}})$ and $0.4 F_{max}$ $(0.4 F_{w_{100}})$ using linear regression. The torsional stiffness values determined experimentally are effective torsional stiffness values $B_{xy,eff,exp.}$ since the transversal shear deformations are included in the total deformation w measured by the rope extensometer [7]. For all specimens that did not reach a failure load, the corresponding load F_{w100} to reach the unit deformation of $100\ mm$ is used instead of F_{max} to determine the effective torsional stiffness. The evaluation is based on the force method (Eq. (16)) and carried out using Eq. (17) [7, 27].

$$w = \int \frac{m_{xy} \cdot \widetilde{m_{xy}}}{2 \cdot B_{xy}} \cdot dx = \int \frac{F \cdot a \cdot \bar{1} \cdot a}{2 \cdot B_{xy}} \cdot dx \tag{16}$$

$$B_{xy,eff,exp} = \frac{F \cdot a^2}{2w} = \frac{(0.4 F_{max} - 0.2 F_{max}) \cdot a^2}{2 (w_{0.4 F_{max}} - w_{0.2 F_{max}})} \tag{17}$$

$$= \frac{1}{2} \cdot m \cdot a^2$$

In order to compare the results of the numerical models with analytical solutions, out-of-plane shear deformations

have to be taken into account within the analytical derivation of stiffness values. These values are referred being "effective" stiffness values and depend on the loading and equivalent static system. For thick plates and shells, taking into account out-of-plane shear deformations is mandatory (Reissner-Mindlin plate theory). Within this investigations, no comparable thick series ($t \geq 200\ mm$) was investigated. Nevertheless, the analytical approach shall be described in the following, because for NLT the semi-rigid connection—and therefore the low out-of-plane shear stiffness—has to be taken into account also for comparable thin layups:

Analytically, effective torsional stiffnesses ($B_{xy,eff}$) can be determined using the method of consistent deformations (force method) on equivalent static systems. Fig. 12 shows the extended girder grid model. Here, in addition to torsional stiffness, shear and bending stiffnesses are assigned to the girders (dx/dy).
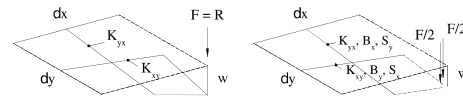

Figure 12: Girder grid model of an infinitesimal element taking into account bending and shear deformations [7]

Following the girder grid model in Fig. 12, the following energy theorem results (Eq. 11):

$$w\delta_{ij} = \int_0^1 \frac{\delta m_{xy} \cdot m_{xy}}{2 K_{xy}} dx + \int_0^1 \frac{\delta m_x \cdot m_x}{B_y} dx \tag{11}$$

$$+ \int_0^1 \frac{\delta m_y \cdot m_y}{B_x} dy + \int_0^1 \frac{\delta V_x \cdot V_x}{S_{xz}} dx + \int_0^1 \frac{\delta V_y \cdot V_y}{S_{yz}} dy$$

The bending and torsional stiffnesses B_x, B_y, and B_{xy} refer to the entries ($D_{11}, D_{22}, and\ D_{66}$) of the *ABD-E* Matrix (Eq. (4)). For CLT and DLT, the shear stiffnesses S_{xz} and S_{yz} can be taken from the entries E_{55} and E_{44}, multiplied by k_z (Eq. (5)). For NLT and DLT_n, S_{xz} and S_{yz} should be determined according to Eq. (6). Based on Eq. (11) the equilibrium of Eq. (12) applies to the total deformation w of the element, taking into account the transverse shear deformations.

$$\frac{F \cdot dx \cdot dy}{B_{xy,eff}} = \frac{F \cdot dx \cdot \bar{1} \cdot dy}{2 D_{66}} + \frac{1}{3} \frac{\frac{F}{2} \cdot dx \cdot \bar{1} \cdot dx}{D_{22}} \tag{12}$$

$$+ \frac{1}{3} \frac{F/2 \cdot dy \cdot \bar{1} \cdot dy}{D_{11}} + \frac{F/2 \cdot \bar{1}}{E_{55}} + \frac{F/2 \cdot \bar{1}}{E_{44}}$$

From this, effective torsional stiffness values are analytically calculated according to Eq. (13).

$$\frac{1}{|B_{xy,eff}|} = \frac{1}{|B_{xy}|} + \frac{1}{6 \cdot |B_x|} + \frac{1}{6 \cdot |B_y|} \tag{13}$$

$$+ \frac{1}{2 \cdot |S_{xz}| \cdot dx} + \frac{1}{2 \cdot |S_{yz}| \cdot dx}$$

Tab. 3 gives the results of the evaluation of the effective torsional stiffnesses from the experimental investigations ($B_{xy,eff,exp.}$) compared to the analytical approaches ($B_{xy,eff}$ and B_{xy}) for each series investigated. For the determination of the analytical solutions, material parameters according to [9; 10; 12] and the effective number of nails according to Tab. 2 are used (see Chapter 2). In this paper the Poisson's ratios according to Halász and Scheer [28] ($\nu_{xy} = 0.380; \nu_{zx} = 0.018$) have been chosen for the calculation of the stiffness matrix. However, when calculating the stiffness properties of CLT and DLT, the chosen values for the Poisson's ratio have no decisive influence.

Table 3: Torsional stiffness of the series following the experimental (mean values in bold) and analytical approach

| | | experimental | analytical | |
| | | $B_{xy,eff,exp.}$ | $B_{xy,eff}$ | [1]B_{xy} |
specimens	series	[MNm²/m]	[MNm²/m]	[MNm²/m]
O1-1		0.159		
O1-2	CLT	0.154		
O1-3	0°, 90°, 0°, 90°, 0°	0.153	**0.155**	0.102	0.115
O1-4	$t = 100$ mm	0.153	COV 2.0	
O2-1		0.013		
O2-2	NLT	0.014		
O2-3	0°, 90°, 0°, 90°, 0°	0.015	**0.014**	0,027	[2]~~0.133~~
O2-4	$t = 105$ mm	0.015	COV 2.3	
O3-1	CLT	0.030	**0.031**		
O3-2	0°, 90°, 0° $t = 60$ mm	0.032	COV 3.5	0.025	0.029
O4-1		0.007		
O4-2	NLT 0°, 90°, 0°	0.008	**0.008**	0.013	[2]~~0.031~~
O4-3	$t = 63$ mm	0.008	COV 3.2	
D1-1		0.023		
D1-2	DLT_n 0°,45°, 90°,−45°,0°	0.023	**0.023**	0.037	[2]~~0.220~~
D1-3	$t = 105$ mm	0.022	COV 3.5	
D2-1		0.019		
D2-2	DLT_n 0°, 30°, 90°, −30°, 0°	0.021	**0.020**	0.036	[2]~~0.199~~
D2-3	$t = 105$ mm	0.018	COV 6.3	
D3-1	DLT	0.201		
D3-2	0°,45°,90°, −45°,0°	0.196	**0.199**	0.134	0.188
D3-3	$t = 100$ mm	0.202	COV 1.6	
D4-1	DLT	0.200		
D4-2	0°, 30°,90°, −30°,0°	0.178	**0.189**	0.122	0.170
D4-3	$t = 100$ mm	0.189	COV 5.6	

[1] values without consideration of transverse shear deformations of the layers
[2] values without consideration of the semi-rigid connection between the layers and without consideration of transverse shear deformations

Compared to the five-layered CLT series O1 with an overall thickness of $t = 100$ mm, the effective torsional stiffness $B_{xy,eff,exp}$ of DLT±45 series D3 is increased by 28.4 %, for DLT±30 series D4 by 21.9 % (mean values). Following the results of the mechanical testing, a considerable ratio of stiffness increase can be determined for DLT_n series with a layer thickness of 21 mm and semi-rigid connected layers, compared to the orthogonal layered NLT series. Compared to the NLT series O2, the effective torsional stiffness of DLT±45_n series D1 can be increased by 76,9 %, for DLT±30_n series D2 by 69.2 % (mean values). The torsional stiffness of the 3-layered orthogonal CLT series O3 is smaller by a factor of 4.94 compared to the 5-layered orthogonal series O1. The DLT_n (series D1 and D2) consisting of five layers can be compared to the NLT consisting of five layers

under 0° and 90° respectively (O2). By rotating the laminations of the 2nd and the 4th layer by ±45 (D1), an increase in torsional stiffness of 90.5 % can be achieved compared to the NLT with five laminations under orthogonal orientation (series O2). By rotating the laminations of the 2nd and the 4th layer by ±60° (series D2), an increase in torsional stiffness of 70.6 % can be achieved compared to series O2 (see Fig. 13).

For the glued CLT and DLT series, the pure torsional stiffness values of (B_{xy}) represent the experimental results better than the analytical values of $B_{xy,eff}$—albeit not significant. This is not surprising, since the application limits/criteria of the calculation theories according to *Kirchhoff-Love* (B_{xy}) and *Reissner-Mindlin* ($B_{xy,eff}$) retain their validity for the rigid DLT and CLT series. To further underline this, additional test results on the torsional stiffness of CLT and DLT from previous studies on DLT [7] are given in Tab. 4. The O5 and D5 series have the same stacking sequence as the O1 and D3 series, but this time with a layer thickness of 40 mm and thus a total thickness of 200 mm, instead of 100 mm.

Table 4: Exemplary additional investigations on the torsional stiffness of the series with t = 200 mm [7]

| | | experimental | analytical | |
| | | $B_{xy,eff,exp.}$ | $B_{xy,eff}$ | [1]B_{xy} |
specimens	series	[MNm²/m]	[MNm²/m]	[MNm²/m]
O5-1		0.898		
O5-2	CLT	0.757		
O5-3	0°, 90°, 0°, 90°, 0°	0.745	**0.791**	0.774	~~0.920~~
O5-4	$t = 200$ mm	0.764	COV 9.1	
D5-1		0.973		
D5-2	DLT 0°,45°,90°, −45°,0°	0.982		
D5-3	0°	0.980	**1.006**	1.007	~~1.502~~
D5-4	$t = 200$ mm	1.089	COV 5.5	

[1]values without consideration of transverse shear deformations of the layers

Without taking the transverse shear deformations into account, the torsional stiffness values B_{xy} fail to represent the experimental values on the thick plate elements. The influence of the out-of-plane shear stiffness and therefore the transversal shear deformation of the 40 mm thick layers are much more pronounced, compared to the series with 20 mm layers. The effective torsional stiffness values $B_{xy,eff}$ on the other hand nearly hit the experimental investigations and confirm the analytical solutions.

When comparing the experimentally determined effective torsional stiffnesses $B_{xy,eff,exp}$ of NLT and DLT_n with the torsional stiffnesses previously derived analytically, it becomes clear that the derived approach for considering transversal shear deformations (Eq. (13)) in combination with Eq. (6) and Eq. (7) leads to satisfactory values for the effective torsional stiffness properties $B_{xy,eff}$. As previously described, values B_{xy}— neglecting both, the out-of-plane shear deformations of the layers and the semi-rigid connection between the layers—are inappropriate to represent the actual/effective torsional stiffness of NLT and DLT_n. The analytical values for $B_{xy,eff}$, on the other hand, can represent the relatively negligible torsional stiffness of the nailed specimens.

5 EXAMPLE OF APPLICATION— DOUBLE SYMMETRIC HP-SHELL

In the following a reference HP-shell from twisted DLT elements is exemplary constructed and calculated. The double symmetric hyperbolic paraboloid to be planned over a square projection has the dimensions $l_x = l_y = 5.30\ m$ and $h_{x'} = h_{y'} = 2.00\ m;\ h = 4.0\ m$. In the context of application-optimized mass timber elements DLT±45°_n elements are used for the construction of the load-bearing structure (ref. to D1 series). The elements remain plane during production and get twisted on site by connecting them to edge beams. Each DLT_n element has a length of about 10.60 m and therefore a width of 1.0 m (without consideration of distortions acc. to Eq. (8)). The plate is loaded with a constant surface load of $p = 3.6\ kN/m^2$ composed by the self weight (lower right, Fig. 13) and snow (upper right side, Fig. 13).
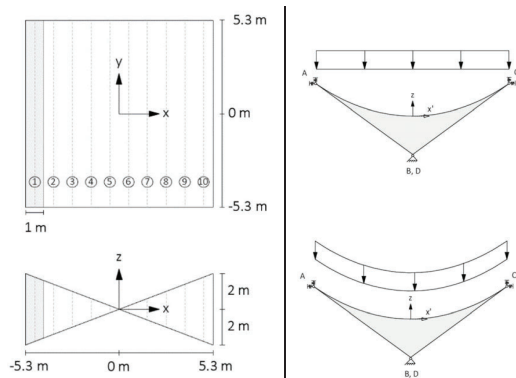

Figure 13: *Ground plan and side view of the HP-shell, divided in sections, representing the DLT elements* [3]

The uniform surface load $p_z = 3.6\ kN/m^2$ leads to in-plane membrane forces n_{xy} in the shell. Therefore, the connections between the elements have to be dimensioned mainly for in-plane shear forces. The connections are fitted on site after twisting the elements by screwing, or dowelling the longitudinal element edges.

The analytical solutions (membrane theory and simplified approaches) according to Chapter 3.2 show in-plane shear forces only ($n_{xy} = 25.28$ kN/m). In order to evaluate the calculation methods, girder grid models are chosen as well as finite element method (FEM) models using the software Dlubal RFEM 5.23 (Quadrangle tool or RF Laminate tool) by inserting the previously calculated *ABD-E* stiffness matrix (Fig. 14).

Figure 14: *FEM shell model created with Dlubal RFEM* [3]

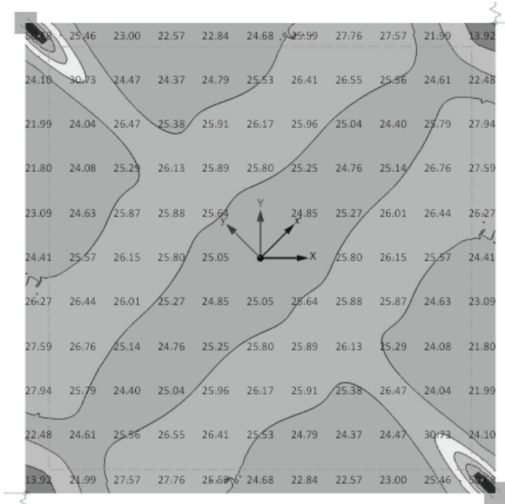Fig. 15 shows the distribution of shear forces n_{xy}.

Figure 15: *Shear forces n_{xy} acting in the calculated with Dlubal RFEM* [3]

The shear forces converge to the solution of the membrane theory ($n_{xy} = 25.28$ kN/m). Bending moments m_x and m_y vanish (extreme values according to the FEM model: $m_x = 0.30\ kNm/m$). With respect to the segmentation and assembly of the shell small torsional moments will occur due to the twisting of the elements on site. These moments should be considered by an additional load case within the model. The torsional stiffness of the elements of D1 series is 0.023 MNm²/m (see Tab. 3). The torsional moment M_T acting within the elements due to the selected element geometry ($w/l = 1.06m/10.6m$) and hights h of the shell is 0.78 kNm—calcualted by Eq. (16). For glued DLT series D3, M_T would appear to be 7.08 kNm. The moment M_T is easily taken by the edge beams (exemplary $w/l = 2 \cdot 0.26m/0.20m$) connected (bolted) to the shell, beyond and above of the edges (Fig. 16).
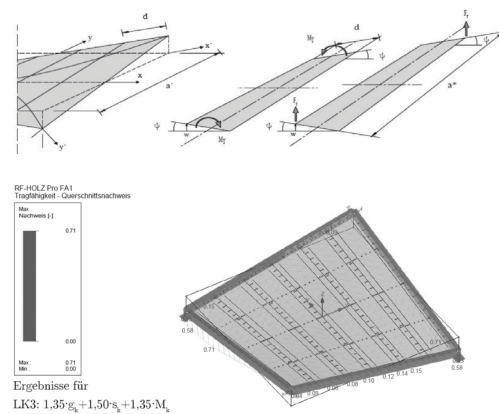

Figure 16: *Torsional moments by twisting the elements (upper sketch) and verification of the load bearing capacity of the beams in the ULS* [30]

As described previously in Chapter 3.2.2, the normal forces acting along the fictive compression and tension parabolas can be calculated by varius simplified methods. For the given example the 4th or 2nd layer of the chosen DLT follows these parabolas providing a high axial rigidity (extensional stiffness) in x´and y´direction. By using these simplified methods, the normal forces within the edge-beams can be estimated without FEM models (Fig. 17).
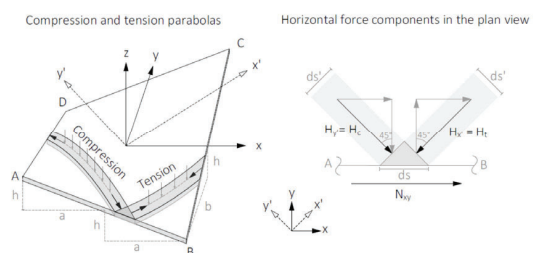

Figure 17: Disassembling of the stress resultants acting on the edge beam according to Parme [3; 24]

As in the entire shell, no bending moments act on the edge beams under the given load—besides the small torsional moments from the twisting of the elements. The surface load results in normal forces N, which are the product of the shear force n_{xy}, multiplied by the length of the edge beams. For the chosen example the normal foces N_x and N_y at the support apper to be 286,4 kN each and are taken by steel connectors and concrete supports.

6 CONCLUSIONS

This paper deals with both, results from the fild of structural analysis and timber engineering, leading to the HP-shell. The HP shell is an architecturally sophisticated, wide-span timber structure that can also be used to roof industrial buildings (Fig. 18). With its structural and architectural relevance, the HP-shell may be brought back into the focus of planners.

Figure 18: Roof structure of the "Silhouette Corset Factory, Market Drayton" made form symmetric timber HP-shells [31]

In addition, the basics of the plate theories according to Kirchhoff-Love and Reissner-Mindlin multi-layered mass timber elements under biaxial bending are applied. This leads to an analytical approach for the determination of the stiffness properties of DLT—with and without consideration of the transverse shear deformations. In addition an analytical approach for the consideration of semi-rigid connected layers of NLT and DLT_n is derived. Extensive series of mechanical experiments are carried out and serve to verify the analytical solutions. At the same time, the test data forms the basis for the calculation and construction of HP-shells using FEM and girder grid models.

Regardless the findings on the sophisticated HP shell structure, the enormous potential of diagonal layer arrangements within mass timber elements becomes obvious. DLT achieves significantly improved torsional properties with the same amount of material. The main outcomes achieved of the experimental investigations are as follows:

- The increase in the effective torsional stiffness of DLT_n elements compared to the NLT elements is undeniable. Compared to the five-layered NLT series with an overall thickness of 105 mm, the effective torsional stiffness $B_{xy,eff}$ of DLT±45_n elements is increased 76.9 % on average. For DLT±30° with t = 100 mm the increase is 69.2 % on average.
- The increase in the effective torsional stiffness of five-layered DLT elements compared to CLT elements with a thickness of 100 mm is 33 % on average for DLT±45°. For DLT±30° with t = 100 mm the increase is 24 % on average.

The investigations show that the torsional stiffness of DLT elements is significantly higher compared to CLT elements. The outcomes of this research render DTL ideal for plates under biaxial bending and concentrated loading, as required for point-supports [32] and promotes a more efficient use of mass timber elements.

REFERENCES

[1] Sprague, T. S.: *Beauty, Versatility, Practicality: the Rise of Hyperbolic Paraboloids in post-war America (1950-1962)*. Construction History, 28 (1), pp. 165–184, 2013.

[2] *Hyperbolisch-parabolische Schale aus Holz*. Bauen + Wohnen, 17 (10), pp. 12–14., 1963.

[3] Fuchs, M.: *Hyperboloidal Roof Structures made of Timber*. Master´s Thesis, Technical University of Munich, 2020.

[4] Farshad, M.: *Design and analysis of shell structures*. Springer Science & Business Media, Luxemburg, 2013.

[5] Candela, F.: S*tructural Applications of Hyperbolic Paraboloidical Shells*. American Concrete Institute, 26, pp. 397–415, 1954.

[6] Bejtka, I.: *Cross (CLT) and diagonal (DLT) laminated timber as innovative material for beam elements*. Karlsruher Berichte zum Ingenieurholzbau, Band 17, KIT Scientific Publishing, Karlsruhe, 2011.

[7] Arnold, M.; Dietsch, P.; Maderebner, R.; Winter, S.: *Diagonal Laminated Timber—Experimental, Analytical, and Numerical Studies on the Torsional Stiffness*. Construction and Building Materials 322, 126455, 2022.

[8] Arnold, M.; Maderebner, R.; Dietsch, P.; Winter, S.: *Diagonallagenholz (DLH): Ressourceneffizienz durch diagonale Orientierungen einzelner Lagen. Teil 1: Bestimmung der Steifigkeitsparameter und Verformungsanalysen*. Under review for Bautechnik, Sonderheft Holzbau,2023.

[9] *ETA-20/0023*, European Technical Assessment. Pfeifer CLT Brettsperrholz. Österreichisches Institut für Bautechnik (OIB), Vienna, 2020.

[10] *ETA-16/0055*, European Technical Assessment. Radiusholz. Österreichisches Institut für Bautechnik (OIB), Vienna, 2020.

[11] *EN 408:2012*: Timber structures – Structural timber and glued laminated timber – Determination of some physical and mechanical properties. CEN – Comité Européen de Normalisation, Brussels, 2012.

[12] *ETA-15/0760*, European Technical Assessment. MHM – Wandelement. Österreichisches Institut für Bautechnik (OIB), Vienna, 2019.

[13] *EN 384:2016*: Structural timber - Determination of characteristic values of mechanical properties and density. CEN – Comité Européen de Normalisation, Brussels, 2016.

[14] Nettles, A.T.: *Basic Mechanics of Laminated Composite Plates*. NASA-RP-1351, NASA Marshall Space Flight Center, 1994.

[15] Schickhofer, G.: *Starrer und nachgiebiger Verbund bei geschichteten, flächenhaften Holzstrukturen. Dissertation*, Verlag der Technischen Universität Graz, 1994.

[16] Timoshenko, S. P.: *On the correction for shear of the differential equation for transverse vibrations of prismatic bars*. The London, Edinburgh and Dublin Philosophical Magazine and Journal of Science, 41:245, 744-746, 1921.

[17] Bogensperger, T.; Silly, G.: *Zweiachsige Lastabtragung von Brettsperrholzplatten*. Bautechnik 91, No. 10, 742-752, 2014.

[18] *DIN EN 1995-1-1/NA:2013-08*, Eurocode 5: Nationaler Anhang - National festgelegte Parameter - Eurocode 5: Bemessung und Konstruktion von Holzbauten - Teil 1-1: Allgemeines - Allgemeine Regeln und Regeln für den Hochbau. Deutsches Institut für Normung (DIN), Berlin, 2013.

[19] Kreuzinger, H.; Scholz A.: *Wirtschaftliche Ausführungs- und Bemessungsmethode von ebenen Holzelementen (Brücken, Decken, Wände)*. Schlussbericht. Institut für Tragwerksbau, Technische Universität München, 1999.

[20] Pucher, A.: *Über den Spannungszustand in gekrümmten Flächen*. Beton und Eisen, 33 (19), pp. 298–304, 1934.

[21] Zingoni, A.: *Shell structures in civil and mechanical engineering. Theory and closed-form analytical solutions*. Thomas Telford Publishing, London, 1997.

[22] Flügge, W.: *Statik und Dynamik der Schalen*. Berlin, Springer-Verlag, 1962.

[23] Flügge, W.; Geyling, F.T.: *A general theory of deformations of membrane shells*. IABSE publications, 17, pp. 24–46, 1957.

[24] Parme, A. L.: *An Elementary Analysis of Hyperbolic Paraboloid Shells-1. Geometrics and Basic Theory*. Indian Concrete Journal, 34 (12), pp. 464–470, 1960.

[25] Hempel, G.: *Hyperbolische Paraboloid-Dächer*. Bauen mit Holz, (10), 479–486. Bruder-Verlag, Karlsruhe, 1967.

[26] Krauss, F.: *Hyperbolisch paraboloide Schalen aus Holz*. Stuttgart, Karl Krämer Verlag, 1969.

[27] Mestek, P.; Winter, S.; Kreuzinger, H.: *Brettstapeln, Brettsperrholz und Verbundkonstruktionen*. Teilprojekt 15 des HTO-Verbundforschungsvorhabens "Holzbau der Zukunft". Technische Universität München, 2008.

[28] Glaser P., Ihler T., Aondio P.: *Untersuchungen zu Segmentschalen aus ebenen Brettsperrholzplatten unter Berücksichtigung nichtlinearer Verbindungseigenschaften*. Der Bauingenieur, VDI Verlag, Düsseldorf, 2020.

[29] Halász, R. von; Scheer, C.: *Grundlagen, Entwurf, Bemessung und Konstruktionen*. Holzbau-Taschenbuch, 9. Auflage. Ernst&Sohn, Berlin, 1996.

[30] Arnold, M.: *Hyperbolische Paraboloid-Schalen aus Brettsperrholz-Theorie, Formfindung & Konstruktion*. Master´s Thesis. Technical University of Munich, 2018.

[31] McCaig, I.; Ridout, B.: *Practical Building Conservation – Timber*. English Heritage, London, 2012.

[32] Arnold, M.: *Mechanical Properties of Diagonal Laminated Timber (DLT) with Respect to Point-Supported Mass Timber Slabs*. Dissertation in progress. Technical University of Munich, expected 2023.